Optimal detection angle in sub-diffraction resolution photothermal microscopy: application for high sensitivity imaging of biological tissues

Jun Miyazaki,[1,2] Hiromichi Tsurui,[3] Koshi Kawasumi,[1] and Takayoshi Kobayashi[1,2,4,5,*]

[1]*Advanced Ultrafast Laser Research Center, The University of Electro-Communications, 1-5-1 Chofugaoka, Chofu, Tokyo, 182-8585, Japan*
[2]*JST, CREST, K' Gobancho, 7, Gobancho, Chiyoda-ku, Tokyo 102-0076, Japan*
[3]*Department of Pathology, Juntendo University School of Medicine, 2-1-1, Hongo, Bunkyo-ku,Tokyo 113-8421, Japan*
[4]*Department of Electrophysics, National Chiao-Tung University, Hsinchu 300, Taiwan*
[5]*Institute of Laser Engineering, Osaka University, 2-6 Yamada-oka, Suita, Osaka 565-0971, Japan*
[*]*kobayashi@ils.uec.ac.jp*

Abstract: We evaluated the optimal detection angle for maximizing the signal to noise ratio (SNR) in sub-diffraction resolution photothermal microscopy. The angular dependent photothermal signal was calculated based on scattering theory using the temporally modulated Yukawa potential, and its detection angle and modulation frequency dependencies were analyzed. We verified the theoretical findings by imaging gold nanoparticles using laser diode based photothermal microscopy with balanced detection scheme. High-sensitivity (SNR ~40) photothermal biological imaging of a mouse brain was also demonstrated.

©2014 Optical Society of America

OCIS codes: (170.5810) Scanning microscopy; (350.5340) Photothermal effects; (100.6640) Superresolution; (290.5825) Scattering theory.

References and links

1. D. Boyer, P. Tamarat, A. Maali, B. Lounis, and M. Orrit, "Photothermal imaging of nanometer-sized metal particles among scatterers," Science **297**(5584), 1160–1163 (2002).
2. S. Berciaud, L. Cognet, G. A. Blab, and B. Lounis, "Photothermal heterodyne imaging of individual nonfluorescent nanoclusters and nanocrystals," Phys. Rev. Lett. **93**(25), 257402 (2004).
3. A. Gaiduk, M. Yorulmaz, P. V. Ruijgrok, and M. Orrit, "Room-temperature detection of a single molecule's absorption by photothermal contrast," Science **330**(6002), 353–356 (2010).
4. C. Leduc, S. Si, J. Gautier, M. Soto-Ribeiro, B. Wehrle-Haller, A. Gautreau, G. Giannone, L. Cognet, and B. Lounis, "A highly specific gold nanoprobe for live-cell single-molecule imaging," Nano Lett. **13**(4), 1489–1494 (2013).
5. V. Octeau, L. Cognet, L. Duchesne, D. Lasne, N. Schaeffer, D. G. Fernig, and B. Lounis, "Photothermal absorption correlation spectroscopy," ACS Nano **3**(2), 345–350 (2009).
6. P. M. R. Paulo, A. Gaiduk, F. Kulzer, S. F. G. Krens, H. P. Spaink, T. Schmidt, and M. Orrit, "Photothermal correlation spectroscopy of gold nanoparticles in solution," J. Phys. Chem. C **113**(27), 11451–11457 (2009).
7. R. Radünz, D. Rings, K. Kroy, and F. Cichos, "Hot brownian particles and photothermal correlation spectroscopy," J. Phys. Chem. A **113**(9), 1674–1677 (2009).
8. C. Leduc, J. M. Jung, R. P. Carney, F. Stellacci, and B. Lounis, "Direct investigation of intracellular presence of gold nanoparticles via photothermal heterodyne imaging," ACS Nano **5**(4), 2587–2592 (2011).
9. S. Lu, W. Min, S. Chong, G. R. Holtom, and X. S. Xie, "Label-free imaging of heme proteins with two-photon excited photothermal lens microscopy," Appl. Phys. Lett. **96**(11), 113701 (2010).
10. D. Lasne, G. A. Blab, S. Berciaud, M. Heine, L. Groc, D. Choquet, L. Cognet, and B. Lounis, "Single nanoparticle photothermal tracking (SNaPT) of 5-nm gold beads in live cells," Biophys. J. **91**(12), 4598–4604 (2006).
11. L. Cognet, C. Tardin, D. Boyer, D. Choquet, P. Tamarat, and B. Lounis, "Single metallic nanoparticle imaging for protein detection in cells," Proc. Natl. Acad. Sci. U.S.A. **100**(20), 11350–11355 (2003).
12. P. Vermeulen, L. Cognet, and B. Lounis, "Photothermal microscopy: optical detection of small absorbers in scattering environments," J. Microsc. **254**(3), 115–121 (2014).
13. L. Wei and W. Min, "Pump-probe optical microscopy for imaging nonfluorescent chromophores," Anal. Bioanal. Chem. **403**(8), 2197–2202 (2012).
14. J. Miyazaki, H. Tsurui, A. Hayashi-Takagi, H. Kasai, and T. Kobayashi, "Sub-diffraction resolution pump-probe microscopy with shot-noise limited sensitivity using laser diodes," Opt. Express **22**(8), 9024–9032 (2014).

15. W.-S. Chang and S. Link, "Enhancing the sensitivity of single-particle photothermal imaging with thermotropic liquid crystals," J. Phys. Chem. Lett. **3**(10), 1393–1399 (2012).
16. A. N. G. Parra-Vasquez, L. Oudjedi, L. Cognet, and B. Lounis, "Nanoscale thermotropic phase transitions enhancing photothermal microscopy signals," J. Phys. Chem. Lett. **3**(10), 1400–1403 (2012).
17. S. Berciaud, D. Lasne, G. A. Blab, L. Cognet, and B. Lounis, "Photothermal heterodyne imaging of individual metallic nanoparticles: Theory versus experiment," Phys. Rev. B **73**(4), 045424 (2006).
18. M. Selmke, M. Braun, and F. Cichos, "Photothermal single-particle microscopy: detection of a nanolens," ACS Nano **6**(3), 2741–2749 (2012).
19. M. Selmke, M. Braun, and F. Cichos, "Gaussian beam photothermal single particle microscopy," J. Opt. Soc. Am. A **29**(10), 2237–2241 (2012).
20. M. Selmke, M. Braun, and F. Cichos, "Nano-lens diffraction around a single heated nano particle," Opt. Express **20**(7), 8055–8070 (2012).
21. M. Selmke and F. Cichos, "Photothermal single particle Rutherford scattering microscopy," Phys. Rev. Lett. **110**(10), 103901 (2013).
22. M. Selmke and F. Cichos, "Photonic Rutherford scattering: A classical and quantum mechanical analogy in ray and wave optics," Am. J. Phys. **81**(6), 405 (2013).
23. H. Yukawa, "On the interaction of elementary particles. I," Proc. Phys.-Math. Soc. Jpn. **17**, 48–57 (1935).
24. K. Gottfried and T.-M. Yan, *Quantum Mechanics: Fundamentals, Second Edition* (Springer, 2003).
25. J. Miyazaki, K. Kawasumi, and T. Kobayashi, "Resolution improvement in laser diodes-based pump-probe microscopy with an annular pupil filter," Opt. Lett. **39**(14), 4219–4222 (2014).
26. K. Uchiyama, A. Hibara, H. Kimura, T. Sawada, and T. Kitamori, "Thermal lens microscope," Jpn. J. Appl. Phys. **39**(9A), 5316–5322 (2000).

1. Introduction

Photothermal microscopy is an efficient method for observing single molecules or nanomaterials using only their optical absorption [1–3]. One of the advantages of photothermal microscopy is that it is less affected by photobleaching, which is the major drawback in fluorescent measurement. By virtue of this fact, it has been used in several biological applications in recent years, such as imaging of live cells using 5nm gold nanoparticles for arbitrarily long periods [4], evaluation of the hydrodynamic properties of cytosol by means of photothermal absorption correlation spectroscopy [5–8], label-free imaging of heme proteins with two-photon excitation [9], and the visualization or tracking of membrane proteins moving at the surface of live cells [10, 11].

Typically in photothermal microscopy, two laser beams with different wavelengths (pump and probe beams) are incident on the sample through a focusing lens. The pump beam increases the temperature around the focal point of the optical absorbing sample. This results in local refractive index variations and induces deflection of the probe beam. The variation of the refractive index with temperature $\partial n / \partial T$ is typically in the order of -10^{-4} K^{-1}, which is readily detected by a lock-in detection scheme as a change in probe beam transmissivity. The pump beam is modulated at 0.1 to 1 MHz and an integration time (the time constant of the lock-in amplifier) of 1-10 ms is used to attain a sufficient signal to noise ratio (SNR) [12]. Thus, the image acquisition time is still slower than that achieved by conventional laser scanning fluorescence microscopy, with an integration time of down to ~1 μs per pixel.

Several technical improvements in photothermal microscopy have increased the SNR. As the relative change in the probe beam transmissivity is detected in a typical experimental setup, it is important to reduce the intensity noise of the beam. To reduce laser noise, a high frequency lock-in detection scheme of over 1 MHz is used, as laser noise is dominant at lower frequencies [13]. Alternatively, an auto-balanced detection scheme can be used for common mode noise reduction at a lower lock-in frequency (up to ~100 kHz) [14]. Using these techniques it is possible to reach shot noise limited sensitivity. It can also be useful to employ an embedding medium with large $\partial n / \partial T$, or media exhibiting a phase transition with large variations of refractive index around the critical temperature [15, 16]. Furthermore, it is important to select the optimal detection angle for the probe beam (the numerical aperture of the condenser lens NA$_c$) to maximize SNR. According to the literature on photothermal microscopy, NA$_c$ is empirically set to be smaller than that of the focusing lens [5, 10, 12, 17, 18]. However, no systematic studies have been conducted to investigate this practice.

In this study, theoretical and experimental analyses were carried out to provide clear understanding of the relationship between the detection angle of the probe beam and the SNR.

High-sensitivity photothermal imaging of a mouse brain was also demonstrated with our sub-diffraction resolution photothermal microscopy, using intensity modulated laser diodes with a balanced detection scheme.

2. Theory

Several models have been proposed to describe the nanoscopic photothermal signal. Selmke and Cichos *et al.* calculated the difference in transmissivity of the focusing probe beam between two steady states, in the presence and absence of the pump beam, using generalized Lorenz-Mie theory [18–20]. They also suggested that the photothermal signal was analogous to Rutherford scattering [21, 22]. However, their model is based on a steady-state calculation and not applicable to the case when thermal diffusion length during one period of the modulating pump beam is comparable to or smaller than the focusing spot size of the probe beam. This condition is considered to be important to attain sub-diffraction resolution as detailed in Sec. 4. Berciaud and Lounis *et al.* provided an analytical description of the photothermal signal, based on the theory of light scattering from a temporally modulating medium [17]. They introduced the time dependent refractive index profile induced by modulation of pump beam intensity, based on the thermal diffusion equation, and derived the photothermal signal intensity from the interference term between the scattering field and an isotropic local oscillator. On the basis of this model, the dependence of the modulation frequency on the photothermal signal was discussed for both forward and backward configurations. However, their plane-wave approximation of the incident probe field did not include the effect of focusing (or transmitted diverging field) on the photothermal signal. As the transmitted field also interferes with the scattered field, it is important to take into account the effect of the focusing field on the photothermal signal.

In this study, we extend these models by considering both the effects of the focusing field and modulating heat sources on the photothermal signal. We consider the case when pump and probe beams are incident on the sample and only the pump beam is absorbed by the point absorber, which then causes an increase in temperature in a surrounding medium. The temperature rise induces an increase or decrease in the refractive index depending on the sign of the thermooptic index and thus the probe beam is deflected. As modulation frequency of the pump beam intensity is much lower than the frequency of the electromagnetic field, we consider the quasi-static Helmholtz equation [21]

$$\nabla^2 U(\mathbf{r},t) + \mathrm{k}^2 [n(\mathbf{r},t)/n_0]^2 U(\mathbf{r},t) = 0, \tag{1}$$

where $U(\mathbf{r},t)$ is the scalar envelope electric field of the probe beam. The refractive index change is related to the temperature rise by $n(\mathbf{r},t) \cong n_0 + (\partial n/\partial T)\Delta T(\mathbf{r},t)$, where n_0 is the refractive index without temperature change. The excitation laser intensity is modulated with frequency of Ω and heat absorbed by the material is given by $\sigma I_0(1 + \cos\Omega t)$, where σ is the absorption cross-section at the pump laser wavelength and I_0 is the beam intensity at the focal point. Assuming that the size of the heat absorber is much smaller than the focal spot size, the temperature profiles can be described by using the heat point source model [11, 17]

$$\Delta T(\mathbf{r},t) = \frac{\sigma I_0}{4\pi\kappa} \left[\frac{1}{r} + \frac{1}{r}\exp\left(-\frac{r}{r_c}\right)\cos\left(\Omega t - \frac{r}{r_c}\right) \right]. \tag{2}$$

Here κ is the thermal conductivity, $r_c = \sqrt{2D/\Omega}$ is the characteristic length for thermal diffusion during one period with D, the thermal diffusion coefficient, and r is the distance from the point heat source. Substitution of Eq. (2) into Eq. (1) reads

$$\nabla^2 U(\mathbf{r},t) + \mathrm{k}^2 [1 + W(\mathbf{r},t)]^2 U(\mathbf{r},t) = 0, \tag{3}$$

where

$$W(\mathbf{r},t) = \frac{\sigma I_0}{4\pi\kappa}\left[\frac{1}{r} + \frac{1}{r}\exp\left(-\frac{r}{r_c}\right)\cos\left(\Omega t - \frac{r}{r_c}\right)\right]. \tag{4}$$

Equation (3) is equivalent to the quasi-static Schrödinger equations, where $W(\mathbf{r},t)$ corresponds to the potential field. The first term on the r.h.s. of Eq. (4) decays with the inverse of radial distance and corresponds to the Coulomb potential in quantum mechanical treatment. The Coulomb potential is effective over a greater distance. The second term is sinusoidally modulated and the amplitude $(1/r)\exp(-r/r_c)$ approaches zero at r_c. This factor is equivalent to the Yukawa potential (the screened Coulomb potential), which was introduced to describe strong nuclear force between nucleons in particle physics [23]. The Yukawa potential coincides with the Coulomb potential in the limit $r_c \to \infty$. In photothermal microscopy, the first term can be regarded as the interaction with the temporally averaged (static) point heat source, whereas the second term is the interaction with the modulated point heat sources and thus the interaction length should be smaller than r_c.

The asymptotic solution of Eq. (3) in the far-field region for an incident plane wave reads

$$\lim_{r\to\infty} U_{\mathbf{k}}(\mathbf{r},t) \sim e^{i\mathbf{k}z} + \frac{e^{i|\mathbf{k}|r}}{r}f_{\mathbf{k}}(\theta,t), \tag{5}$$

where $\mathbf{k}$ denotes the wave vector of the incident plane wave and $f_{\mathbf{k}}(\theta, t)$ is the scattering amplitude, with θ the angle between $\mathbf{k}$ and the scattering field wave vector $\mathbf{k}_{sc}$ as pictured in Fig. 1. The scattering amplitude is calculated under the first-order Born approximation as

$$f_{\mathbf{k}}^{(1)}(\theta,t) = -\frac{1}{4\pi}\int W(\mathbf{r}',t)e^{i\Delta\mathbf{k}\cdot\mathbf{r}'}d\mathbf{r}'$$
$$= -\frac{\sigma I_0}{8\pi\kappa n_0}\frac{\partial n}{\partial T}\left[\frac{2}{|\Delta\mathbf{k}|^2} + \frac{2|\Delta\mathbf{k}|^2}{|\Delta\mathbf{k}|^4 + 4/r_c^4}\cos(\Omega t) + \frac{4/r_c^2}{|\Delta\mathbf{k}|^4 + 4/r_c^4}\sin(\Omega t)\right] \tag{6}$$

with $|\Delta\mathbf{k}| = |\mathbf{k} - \mathbf{k}_s| = (4\pi n_0/\lambda)\sin(\theta/2)$. The first term in the square bracket of Eq. (6) corresponds to the scattering amplitudes due to the Coulomb potential. The second and the third terms correspond to the scattering amplitude due to the temporally modulated Yukawa potential and their sum can be written as $2r_c^2/\sqrt{u^2+1}\cos(\Omega t - \tilde{\Phi})$, where $\tilde{\Phi} = \tan^{-1}(1/u)$ is the phase shift with $u = |\Delta\mathbf{k}|^2 r_c^2/2$. The scattering cross section, defined as the ratio of angularly integrated scattered field intensity to that of the incident field intensity, is given by

$$\sigma_{sc}(t) = 2\pi\int_0^\pi \left[f_k^{(1)}(\theta,t)\right]^2\sin\theta d\theta$$
$$= \frac{4\pi}{k}\mathrm{Im}\, f_k^{(2)}(0,t). \tag{7}$$

The conservation of the probability requires that $\sigma_{sc}(t)$ is related to the imaginary part of the scattering amplitude under second-order Born approximation (optical theorem) [24]. When the incident and deflected (scattered) photons are collected through a condenser lens with $NA_c = n_0\sin\varphi_c$ in the far field, as depicted in Fig. 1, the fraction of photons deflected outside the condenser lens (the residual scattering cross section) is expressed as

$$\Sigma(\varphi_c,t) = \sigma_{sc}(t) - 2\pi\int_0^{\varphi_c}\left[f_k^{(1)}(\theta,t)\right]^2\sin\theta d\theta, \tag{8}$$

where the second term on the r.h.s of Eq. (8) is the fraction of photons deflected in the angle lower than φ_c. We note that the residual scattering cross section is zero when photons are collected in all angles, i.e., $\Sigma(\pi, t) = 0$.

In photothermal microscopy, the focusing beam is incident on the sample through an objective lens and thus we consider a super-position of Eq. (5) at multiple incident angles to examine the effect of the focusing field on the photothermal signal

$$U(\mathbf{r}, t) = \int d\mathbf{k} A(\mathbf{k}) U_{\mathbf{k}}(\mathbf{r}, t) \sim U_{inc}(\mathbf{r}) + U_{sc}(\mathbf{r}, t). \tag{9}$$

Here,

$$U_{inc}(\mathbf{r}) = \int d\mathbf{k} A(\mathbf{k}) e^{i\mathbf{k} \cdot \mathbf{r}} \tag{10}$$

denotes the incident focusing field and

$$U_{sc}(\mathbf{r}, t) = \frac{e^{i|\mathbf{k}|r}}{r} \int d\mathbf{k} A(\mathbf{k}) f_{\mathbf{k}}(\theta, t) \tag{11}$$

is the scattered field. For example, for an azimuthally symmetric and uniform intensity spherical wave focusing at $\mathbf{r}_0$, with $NA_f = n_0 \sin\varphi_f$, the amplitude factor $A(\mathbf{k})$ is expressed by

$$A(\mathbf{k}) = \begin{cases} e^{-i\mathbf{k}\mathbf{r}_0} / |\mathbf{r} - \mathbf{r}_0| & \text{for } \varphi' \leq \varphi_f, \\ 0 & \text{for } \varphi' > \varphi_f, \end{cases} \tag{12}$$

where φ' is the polar angle of $\mathbf{k}$. By assuming that $f_k(\theta, t) \ll 1$, the square of the scattering field is negligibly small, and in this case, interference between the scattered field and the transmitted field is dominant. Thus, we approximate the scattering cross-section as an intensity ratio of the integrated interference signal to the incident beam intensity

$$\sigma_{sc}'(t) = J_{sc}(\pi, \text{t}) / J_{inc}(\pi), \tag{13}$$

where

$$J_{sc}(\varphi, \text{t}) = (1/2) \left\lfloor 2\pi \int_0^\varphi U_{sc}(\mathbf{r}, t) U_{inc}(\mathbf{r})^* \sin\theta d\theta + c.c. \right\rfloor$$
$$J_{inc}(\varphi) = 2\pi \int_0^\varphi U_{inc}(\mathbf{r}) U_{inc}(\mathbf{r})^* \sin\theta d\theta. \tag{14}$$

When the incident and deflected photons are collected through a condenser lens in far-field region, the photothermal signal is proportional to

$$\Sigma'(\varphi_c, t) = \left\lfloor \sigma_{sc}'(t) J_{inc}(\varphi_c) - J_{sc}(\varphi_c, \text{t}) \right\rfloor / J_{inc}(\pi), \tag{15}$$

where the first term on the r.h.s of Eq. (15) refers the fraction of photons that have incident angle lower than φ_c and undergo scattering, while the second term is the fraction of the scattered photons in the angle lower than φ_c. Here, we assumed that the incident field is focused at the position of the point light absorber. The scattering amplitude is given by the sum of the three terms in Eq. (6), so Eq. (15) can be rewritten separately as

$$\Sigma'(\varphi_c, t) = C(\varphi_c) + Y_{in}(\varphi_c) \cos(\Omega \text{t}) + Y_{out}(\varphi_c) \sin(\Omega \text{t}), \tag{16}$$

where $C(\varphi_c)$ is attributable to the first term (the Coulomb potential), and $Y_{in}(\varphi_c)$ and $Y_{out}(\varphi_c)$ to the second and third terms (the temporally modulated Yukawa potential), respectively. In a

typical photothermal experiment, the pump beam intensity is modulated and the resulting change in the probe beam transmissivity is detected by a dual-phase lock-in amplifier. In this case, $Y_{in}(\varphi_c)$ and $Y_{out}(\varphi_c)$ are measured as in-phase and $\pi/2$ as out-of-phase components, respectively.
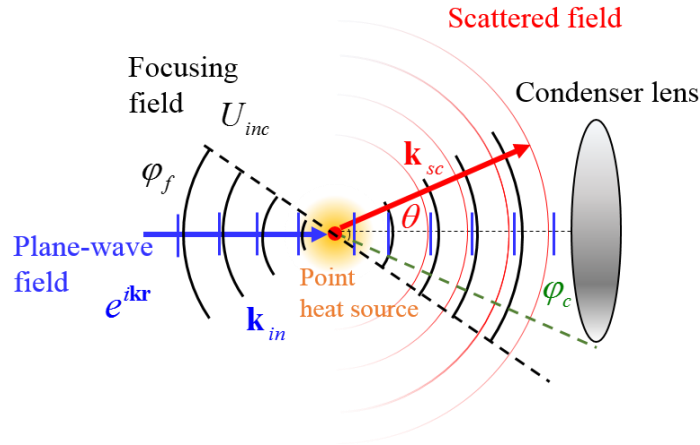

Fig. 1. Schematic illustration of the principle of photothermal microscopy. A plane-wave field (blue lines) or a focusing field with $NA_f = n_0 \sin \varphi_f$ (black curves) is incident on the sample and is deflected (scattered) due to the local refractive index change around a point heat source. Transmitted and deflected photons are collected through a condenser lens with $NA_c = n_0 \sin \varphi_c$.

Figure 2(a) shows Y_{in} and Y_{out} as a function of NA_c. Their magnitude $M = \sqrt{Y_{in}^2 + Y_{out}^2}$ and the phase $\Phi = \tan^{-1}\left[Y_{out}/Y_{in}\right]$ of the output are also shown for the set of $|\Delta\mathbf{k}| = 2$, $n_0 = 1$, and $NA_f = 0.95$. It is important to note that the magnitude has a peak at $NA_c = 0.73$ and is zero for $NA_c > NA_f$. Thus, NA_c should be smaller than that of the focusing lens to achieve optimal SNR. We also note that the sign of Y_{in} is negative for a negative $\partial n/\partial T$, which suggests that transmissivity increases in the presence of the pump beam. This is because the wide-angled incident field component, with $\varphi' > NA_c$, is deflected to the angle lower than NA_c and thus contributes to the positive signal gain. We found that the peak position of Y_{in} is smaller than that of Y_{out}, and so Φ has a tendency to increase with φ_c. Figure 2(b) shows angular dependence of M for several values of r_c. We found that the peak value decreases and the peak position slightly shifts to the lower angular side as r_c decreases.
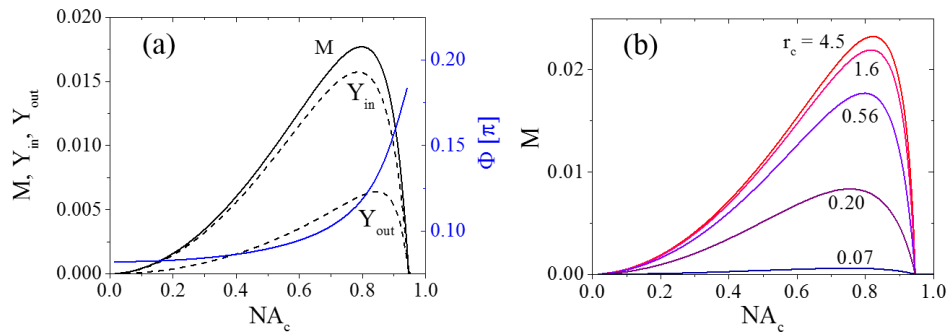

Fig. 2. Detection angle dependence of the photothermal signal. (a) Y_{in} and Y_{out} as a function of numerical aperture of the condenser lens NA_c. We set $r_c = 0.56$. The vertical axis is normalized by $(\sigma I_0)/(8\pi\kappa n_0)\partial n/\partial T$. Their magnitude M and the phase shift Φ are shown as black and blue solid lines, respectively. (b) M as a function of NA_c with various values of r_c.

3. Experiments

Detection angle dependence of the photothermal signal was examined experimentally in our pump-probe microscopy system, which uses intensity modulated laser diodes (LDs) and a balance detector. The details have been described previously [14]. We used a 488 nm LD for the pump, and a 640 nm LD for the probe beam. Each beam was collimated through a spatial filter and two beams were combined using dichroic mirrors. The probe and pump-beam intensities were typically modulated at frequencies of ω_1 and ω_2, respectively. A beat signal $|\omega_1-\omega_2|$ is generated by the bilinear interaction of the pump field and the probe field in the sample. We used a lock-in technique to detect the signal, and the lock-in amplifier was referenced to the beat frequency. By changing the modulation frequencies (ω_1 and ω_2) while holding the difference frequency $|\omega_1-\omega_2|$ constant, this dual modulation scheme has the potential to acquire time-resolved information without a high-speed detector. To counteract the intensity fluctuation of the probe laser, we split the probe beam into two and directed the two resulting beams to an auto-balanced photodetector (New Focus, Nirvana). This auto-balanced detector serves to cancel both the laser noise and the intensity imbalance due to refractive index variations during the sample scanning. We confirmed that when the probe beam power incident on the photodiode was above ~10 μW, the signal to noise ratio was mainly limited by shot noise. The pump and probe beams were linearly polarized. A polarizing beam splitter (PBS) was used to direct the combined beam to the objective lens (UPLSAPO 40X2, Olympus) with numerical aperture NA_f of 0.95. The beam size was adjusted to fill the back aperture of the objective lens. The sample position was raster scanned using a three-axis positioning stage driven by piezo actuators (MAX311D, Thorlabs or P-622.2, PI). A condenser lens with variable NA_c (U-AAC, Olympus) was used to collect the transmitted light. This lens is equipped with a diaphragm for varying NA_c. The maximum value of NA_c was 1.4 with immersion oil, while it was ~0.95 without immersion oil. In this study, immersion oil was not employed since a dry objective was used for focusing the probe beam. The distance between the glass substrate and the front side of the condenser lens was ~0.5 mm. A narrowband filter matching the laser line was placed in front of the detector to filter out the pump beam, so that only the probe beam was detected. The pump and probe beams were collimated so that they focused at the same position.

We measured the photothermal signal from 20 nm diameter gold nanoparticles dispersed in a polyvinyl alcohol (PVA) film on a glass slide with varying NA_c (Fig. 3). The wavelength of the pump beam overlapped the absorption spectrum of the gold nanoparticles as the plasmon resonance peaked at 524 nm. The pump and probe powers incident on the sample were 0.7 mW and 0.3 mW, respectively and were modulated at 1.015 MHz and 1.000 MHz, respectively. The time constant of the lock-in amplifier was 0.5 ms and the pixel dwell time was 1 ms. We found that the full width at half maximum (FWHM) value of a single particle is ~240 nm, which is 19% smaller than the diffraction limited spot size of the pump beam and 32% smaller than that of the probe beam [25]. Furthermore, the axial spot size was 590 nm, which is 33% smaller than the diffraction-limited axial size of the probe beam. Upper and lower panels of Fig. 3 show magnitude, M, and phase shift, Φ, images, respectively, with several values of NA_c. Since the thickness of the PVA film is about 20 μm, gold nanoparticles are distributed in both lateral and axial direction. This leads to the signal intensity distribution of gold nanoparticles in the xy-image. To characterize the images, we calculated the integrated intensity of M and the average Φ for each image, summarized in Fig. 4(a). It is important to note that with increasing NA_c, integrated intensity increases and then decreases when NA_c is larger than ~0.4, while Φ monotonically increases with NA_c. These tendencies are in accordance with the theoretical calculation as shown in Fig. 2(a). Furthermore, we evaluate the effect of NA_c on the signal to noise ratio (SNR) to ascertain the optimal NA_c. To this end, the maximum value S_{max} and the root mean square (r.m.s.) of background level S_b are calculated for each image. Figure 4(b) shows S_{max}, S_b, and their ratio S_{max}/S_b as a function of NA_c. We found that S_{max} has a peak at $NA_c = 0.45$, while S_b increases with increase in NA_c, as an increase in the beam power incident on the detector is accompanied by an increase in noise

power. Consequently, S_{max}/S_b has a maximum value of 60 at NA_c ~0.4 and significantly decreases to 12 at $NA_c = 0.85$. We calculated maximum intensity S_{max} instead of the mean intensity S_{mean} because it is difficult to determine the latter due to the background noise that is prominent for a large NA_c. However, we found that S_{mean} gives similar trend as S_{max}. We also checked the modulation frequency dependence on the signal intensity and found that the signal intensity decreases by approximately half when the modulation frequency reaches 2 MHz. This agrees with the experimental results in the literature [1, 2]. We also measured the incident beam power dependence and found that the signal is proportional to the product of the pump and probe power. These facts verify that the measured signal is to be attributed to the photothermal effect.
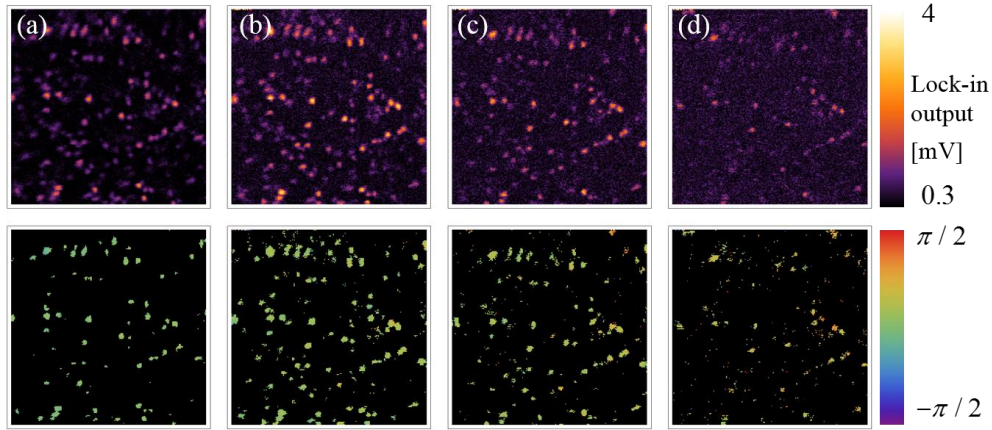

Fig. 3. Magnitude (upper panel) and the corresponding phase shift images (lower panel) of gold nanoparticles dispersed in PVA film. The numerical aperture of the condenser lens NA_c was (a) 0.3, (b) 0.42, (c) 0.54, and (d) 0.66. The image size is 19.6 x 19.6 μm with 200 x 200 pixels.
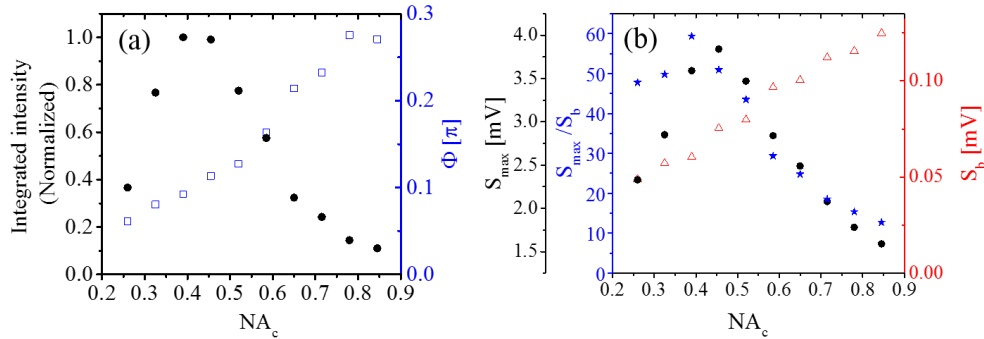

Fig. 4. (a) The integrated intensity (filled black circles) and average phase shift, Φ, (open blue squares) as a function of the numerical aperture of the condenser lens (NA_c). (b) Maximum intensities in the images S_{max} (filled black circles) and background noise levels S_b (open red triangles), and their ratios (blue stars) as a function of NA_c.

Biological photothermal imaging was demonstrated using mouse brain labeled with weakly fluorescent quantum dots (Fig. 5). The brain of a two month old C57BL/6 mouse was embedded in O.C.T. compound (SAKURA Seiki Co. Ltd., Tokyo Japan), frozen in liquid nitrogen, sliced at 14 μm, and air-dried. Sections were stained with anti-α-tubulin antibody labeled with eFluor 650NC (eBioscience, CA, San Diego), mounted on coverslips, and imaged. The samples were placed under atmospheric conditions for several months to induce surface oxidization of quantum dots, where rapid non-radiative exciton decay due to charge recombination dominates the relaxation pathway and photo excitation energy is mainly

converted to heat. The pump and probe beam power were 4 mW and 0.6 mW, respectively. The time constant of the lock-in amplifier was 0.5 ms and the pixel dwell time was 1 ms. Pump and probe beams were modulated at 1.1 MHz and 1.0 MHz, respectively. Figure 5(a) shows an overview image with the image size of 200 x 200 μm. Figures 5(b)–5(d) show a set of images with different values of NA_c. It can be clearly seen in Figs. 5(b)–5(d) that the largest SNR is attained for $NA_c = 0.36$ [Fig. 5(b)]. The calculated values of S_{max}/S_b were (b) 40, (c) 17, and (d) 6. We confirmed that there was minimal damage to the sample after measurements. It is possible that stimulate emission contributed to the lock-in signal, as the laser wavelength overlapped the fluorescence of the quantum dot peak at 650 nm [14]. However, we consider the photothermal signal is a majority component because the detected signal significantly decreases for a large NA_c.
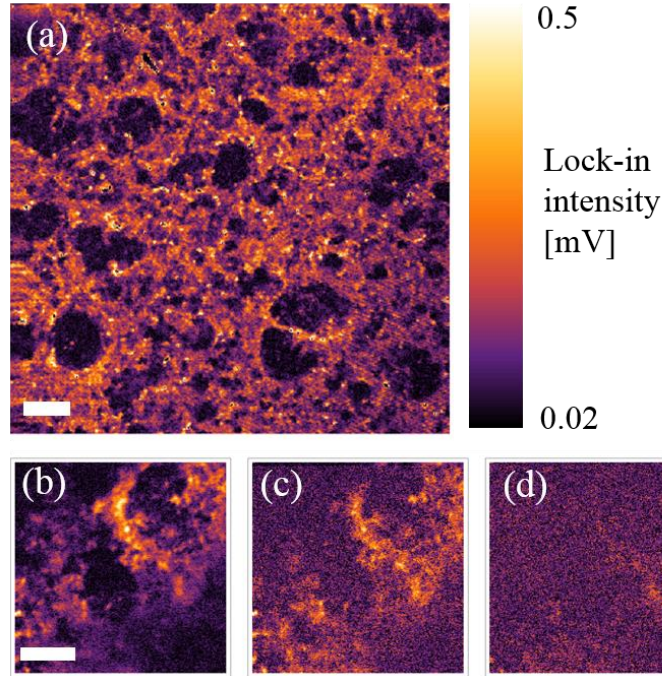

Fig. 5. Photothermal imaging of a slice of mouse brain labeled with weakly fluorescent quantum dots. (a) Overview image and (b)-(d) images of the same area with different values of the numerical aperture of the condenser lens NA_c. The image sizes are (a) 200 x 200 μm with 500 x 500 pixels and (b)-(d), 19.6 x 19.6 μm with 200 x 200 pixels. NA_c was set at (a) 0.42, (b) 0.36, (c) 0.72, and (b) 0.9, respectively. The scale bars indicate (a) 20 μm and (b) 5 μm.

4. Discussion and conclusion

In this study, theoretical and experimental analyses were carried out to ascertain the optimal detection angle for the probe beam to maximize SNR. We found that signal intensity significantly depends on NA_c. The magnitude of the photothermal signal has a maximum value when $NA_c = 0.4$, which is less than half that of the focusing lens of $NA_f = 0.95$. We also confirmed that the phase shift, Φ, increases as NA_c increases. These trends qualitatively agree with the theoretical calculation in which the photothermal signal has a maximum value in the region $NA_c < NA_f$, while it is zero for $NA_c > NA_f$. However there are several discrepancies between the experimental data and theoretical calculations. In the experimental data, the photothermal signal remains even when $NA_c \sim NA_f$, although the SNR is small. This is probably attributable to the static scattering field, such as Rayleigh scattering by a gold nanoparticle or light scattering at the surface of the glass plate, which serves as a local oscillator and causes interference with the temporary modulated scattering filed [17]. In the present study, signal was detected in the forward direction, and thus we approximated that the

photothermal signal mainly comes from the interference between temporally modulated scattering field and the diverging transmitted probe field. This makes the signal to vanish for $NA_c > NA_f$ in the theoretical calculation. On the other hand, for the backward detection, the photothermal signal may be attributable to the interference between the static scattering field and the temporally modulated scattering field. In that case, signal intensity should be proportional to the square of NA [6].

The peak position of the photothermal signal also differs between the experimental data and the theoretical calculations. In this regard, we examined how the theoretical curve of M depends on the parameters, and found that the optimal value of NA_c (position of the maximum M) decreases as λ or the focal spot size increases, while it increases with NA_f. Furthermore, we assume uniform probe beam at the pupil of the focusing lens in theoretical calculations. However, experimentally, the incident beam is a Gaussian beam truncated by the limiting aperture of the objective pupil. For a Gaussian beam focusing at the sample position $A(\mathbf{k}) = \exp(-\varphi'^2/2\sigma^2)$ with $\sigma = 0.1\pi$, the optimal value appears at $NA_c \sim 0.3$. However, Φ decreases as NA_c increases. Further study is needed in regard to this point including the effect of the focal position on the signal.

Theoretical analysis and experiments were carried out for a particle whose diameter is much smaller than wavelength of visible light (20-nm Au nanoparticle and 5-nm quantum dot), since a smaller particle is usually more preferred for a probe molecule in biological imaging. For a large particle, it is expected that forward static scattering field also interferes with the modulated scattering field, which gives a similar result as in the case of the transmitted probe field. In this regard, in images of the slice of mouse brain, we observed several spots with the sizes from several hundred nm to ~1 μm due to the aggregates of quantum dots. We found that signal intensities from these spots also decrease for a large NA_c. This suggests that the optimal NA_c is smaller than NA_f regardless of the size of nanoparticles.

In a conventional thermal lens model, change in probe beam transmissivity is explained by considering the deflection by a concave lens induced by the temperature rise. This picture may be valid when r_c is larger than the focal spot size. In such a case, the temporally modulated Yukawa potential in Eq. (4) is approximated by the Coulomb potential, and consequently the photothermal signal is described in a similar manner to Rutherford scattering [21, 22] or by a lens-like model [18, 20]. In the present experiment, by assuming the thermal diffusivity of 0.1 mm^2/s and the modulation frequency of the pump beam of 1 MHz, r_c is estimated to be ~0.1 μm, which is about four times smaller than the calculated focal spot size of the probe beam ($0.61\lambda/NA_f = 410$ nm). In this regard, it is interesting to examine the spatial resolution with changing modulation frequencies, because when r_c is much smaller than the focal spot size, the spatial resolution (the point spread function) should be determined by the product of the pump and probe beam intensity at the focal point. In this case, spatial resolution improves [14, 25]. The improvement of the spatial resolution is attributed to the fact that the photothermal signal is based on the nonlinear interaction between the two laser beams and the sample. In contrast, it is expected that the spatial resolution is determined by a pump beam intensity distribution when r_c is much larger than the focal spot size. It is also important to examine the z-dependence of the photothermal signal with varying r_c. In a thermal lens model, signal intensity exhibits two peaks that correspond to focusing or defocusing when the sample position is moved in the axial direction [26]. However, in the present study, the amplitude of the lock-in signal exhibited only a single peak and the phase was nearly flat and did not exhibit the π shift at the origin. Further investigation is needed to clarify the modulation frequency dependence on the photothermal signal.